Artificial-Intelligence-Enabled Real-Time Calibration of Scanning Microwave Microscopy

Yawei Zhang[1],Xiaopeng Wang[1], Marco Farina[1,3], James C.M. Hwang[1], Yunyue Zhu[2],Nannan Mao[2], Peng Wu[2], Jing Kong[2]
[1]Cornell University, Ithaca, NY, USA
[2]Massachusetts Institute of Technology, Cambridge, MA, USA
[3]Polytechnical University of Marche, Ancona, Italy
[1]yz2954@cornell.edu, [2]yunyue@mit.edu, [3]m.farina@staff.univpm.it

***Abstract*—Scanning microwave microscopy (SMM) uses near-field microwave radiation for non-destructive subsurface material characterization of both structural and electrical properties on the nanoscale. However, its widespread adoption is hindered by complicated post-measurement data processing, which involves solving the inverse problem by trial-and-error fitting of measured scattering parameters to 3D finite-element-simulated electromagnetic responses based on assumed material properties. Furthermore, existing calibration techniques often fail to account for the wear of the delicate and sensitive SMM probe. To overcome these challenges, this work introduces a substrate-referenced deep-learning algorithm with sufficient artificial intelligence to automatically solve the problem in real time. By decoupling dynamic probe geometry from static substrate parasitics, a machine-learning regressor chain precisely infers from a single approach curve error coefficients with a root-mean-square error to the fourth decimal place (0.0086 in the present case). This approach has been validated on 2D SnSe flakes of different thickness on different substates. This shows that for the first time, real-time quantitative SMM imaging of material properties without the operator being an expert in computational electromagnetics.**

***Keywords*—Artificial intelligence, atomic force microscopy (AFM), calibration, machine learning, tin selenide, two-dimensional materials, scanning microwave microscopy (SMM)**

I. Introduction

With the fast growth of nanotechnology and two-dimensional (2D) atomic-layered materials, it has been challenging to use conventional material characterization techniques to determine their structural or electrical properties. To overcome the challenges, scanning microwave microscopy (SMM) has emerged as a critical tool bridging the gap between microwave engineering and nanotechnology. By combining the structural sensitivity of atomic force microscopy (AFM) with the electrical sensitivity of a vector network analyzer (VNA), SMM offers unparalleled capabilities for non-destructive subsurface characterization of nanomaterials, including semiconductors, dielectrics, and biological cells [1]–[11]. However, despite its great potential, the widespread adoption of SMM is stifled by complicated post-measurement data processing.

Conventionally, an SMM image is made of the magnitude or phase of the microwave reflection coefficient S_{11}, which is a convolution of material properties, setup parasitics, and probe geometry. Solving such a complicated inverse problem involves trial-and-error assumptions of sample structure and property and fitting their 3D-finite-element-simulated electromagnetic responses to the measured S_{11}. This requires substantial computational expertise, power, and time. This also makes it impossible to visualize in real time intrinsic material properties, preventing the operator from homing in on regions of interest such as defect regions.

To overcome these challenges, this work presents a substrate-referenced machine-learning calibration that automatically solves the inverse problem of SMM. We propose a split calibration that decouples the calibration into two distinct components: static substrate parasitics and dynamic probe geometry. The former can be inferred by the characteristics of the probe as it approaches the substrate without a sample; the latter can be inferred in real-time by machine learning involving training with experimental data augmented by physics-informed domain randomization. This divide-and-conquer approach allows the SMM to image intrinsic material properties in real time, thereby transforming SMM into an accessible, high-throughput metrology tool.

II. Method

A. SnSe Sample

2D SnSe flakes are synthesized using low-pressure physical vapor deposition [12]. The synthesis begins by placing SnSe powder precursor in a crucible at the center of a tube furnace. A freshly exfoliated mica substrate, annealed at 400 °C in air for 10 min, is positioned 10-cm downstream from the precursor. The furnace is then evacuated to 10 mTorr and heated to 420 °C for a deposition of approximately 40 min. After deposition, the furnace is quickly cooled to room temperature. The synthesized SnSe flakes are up to 23-μm wide and 2–175 nm thick. Finally, using polymethyl methacrylate, SnSe flakes are transferred from mica to doped-Si substrates with and without a surface coating of 300-nm-thick SiO_2. The region between the flakes where the Si substrate is exposed can be used for SMM calibration.

B. SMM Setup

Fig. 1. illustrates the SMM/AFM setup. It is based on a Keysight Technologies 7500 AFM equipped with an N9545C SMM nose cone [9]. 25 nm Mountain 25Pt300A platinum probe, featuring a spring constant of 18 N/m and a tip radius of

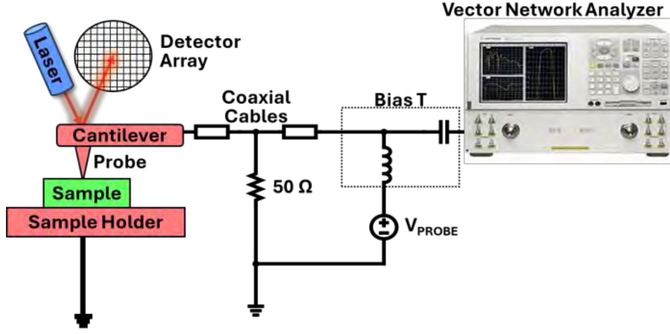

Fig. 1. Schematics of the AFM-based SMM.

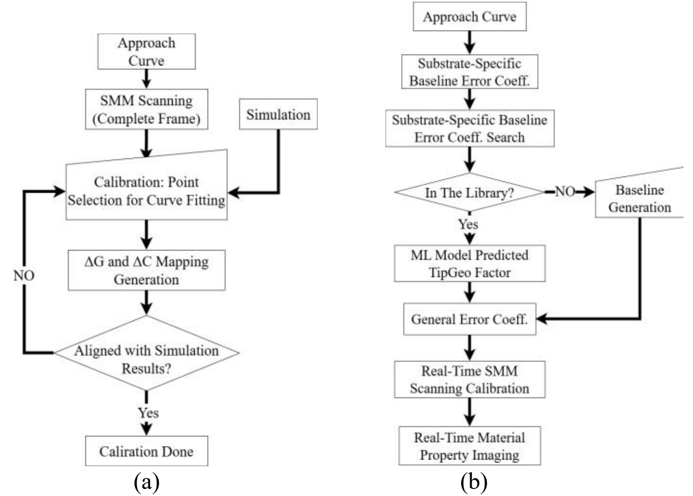

Fig. 2. Flowcharts of (a) manual vs. (b) automated SMM calibrations.

25 nm, serves as the dual-function AFM/SMM probe. This probe is affixed to a platinum cantilever 300-μm long, 60-μm wide, and 2-μm thick. The cantilever is connected to a Keysight Technologies E8062B vector network analyzer (VNA) via coaxial cables. For impedance matching around 3 GHz and its harmonics, the cables are shunted with a 50 Ω resistor.

For SMM, the VNA generates a 0-dBm signal at resonance frequency in the GHz range, which incidents from the probe to the sample. This power level is selected to provide an adequate signal-to-noise ratio (SNR) while minimizing sample destruction. Within the 18-GHz bandwidth, 15.7 GHz is chosen to maximize image contrast because the higher the frequency, the higher the sensitivity to small capacitances [2]. The VNA detects S_{11} reflected from the sample following its near-field interaction with the probe. The intermediate frequency bandwidth of the VNA is set to 500 Hz, balancing SNR and scan rate. Under these conditions, a maximum 15 μm × 15 μm area can be scanned at a resolution of 256 × 256 pixels in approximately 4 min, corresponding to a scan rate of 200 pixels/s. During the same scan, SMM and AFM signals are simultaneously detected and recorded.

C. Manual Calibration

Conventionally, S_{11} measured by SMM is converted to the probe-sample interaction admittance Y by one-port *in situ* calibration [1], [4]. The calibration is based on measuring S_{11} as the probe approaches the exposed substrate between SnSe flakes, while measuring the probe-sample capacitance C using the AFM in the mode of electrostatic force microscopy. By acquiring both S_{11}(z) and C(z) as functions of the probe-sample distance z, the error coefficients e_{00}, e_{01}, and e_{11} are extracted as [1]:

$$S_{11,m} = e_{00} + e_{01}\frac{S_{11,a}}{1 - e_{11}S_{11,a}}, \tag{1}$$

where $S_{11,\mathrm{m}}$ is the measured S_{11} and

$$S_{11,a} = \frac{Z_{in} - Z_{ref}}{Z_{in} + Z_{ref}}. \tag{2}$$

The probe geometry, such as the radius of the probe tip and the cone angle/height of the probe body are extracted by fitting C(z) curves with simulated probe characteristics [1]. After S_{11} is converted to Y, it is used to extract the sheet resistance R_{sh} of SnSe flakes using a simple equivalent circuit model validated by numerical simulations [9]. To this end, three-dimensional finite-element electromagnetic simulations are performed using the COMSOL AC/DC module.

D. Automated Calibration

As illustrated in Fig. 2(a), conventional calibration uses three error coefficients that are highly dependent on the probe geometry, which changes with use. To address this effect and to shorten the overall calibration time and complexity, we propose a split calibration [Fig. 2(b)] that decouples static setup parasitics from dynamic probe geometry.

The first step of split calibration is to determine the static error coefficients ($e_{00}^{base}, e_{01}^{base}, e_{11}^{base}$) associated with the specific substrate material (e.g., SiO_2/Si). These coefficients account for all static signal-path contributions, including cable losses, connector losses, and cantilever capacitance, which static constant for a specific substrate. These baseline error coefficients are extracted from the approach curve to the exposed substrate between SnSe flakes. Then, follow the same procedure as in conventional calibration, the measured C(z) curve is fitted to the theoretical approach curve derived from COMSOL simulations to obtain the static error coefficients. This process is repeated for many approach curves taken at different locations and frequencies from different batches to account for substrate inhomogeneity. Finally, we compute the root-mean-square (RMS) average values to define a robustly define set of static error coefficients.

To account for changes in the probe geometry, we define a dynamic set of error coefficients which transforms the static error coefficients by the probe geometry:

$$\begin{bmatrix} e_{00} \\ e_{01} \\ e_{11} \end{bmatrix} = \begin{bmatrix} e_{00}^{base} \\ e_{01}^{base} \\ e_{11}^{base} \end{bmatrix} \odot \begin{bmatrix} G_{00}^{tip} \\ G_{00}^{tip} \\ G_{11}^{tip} \end{bmatrix} \tag{4}$$

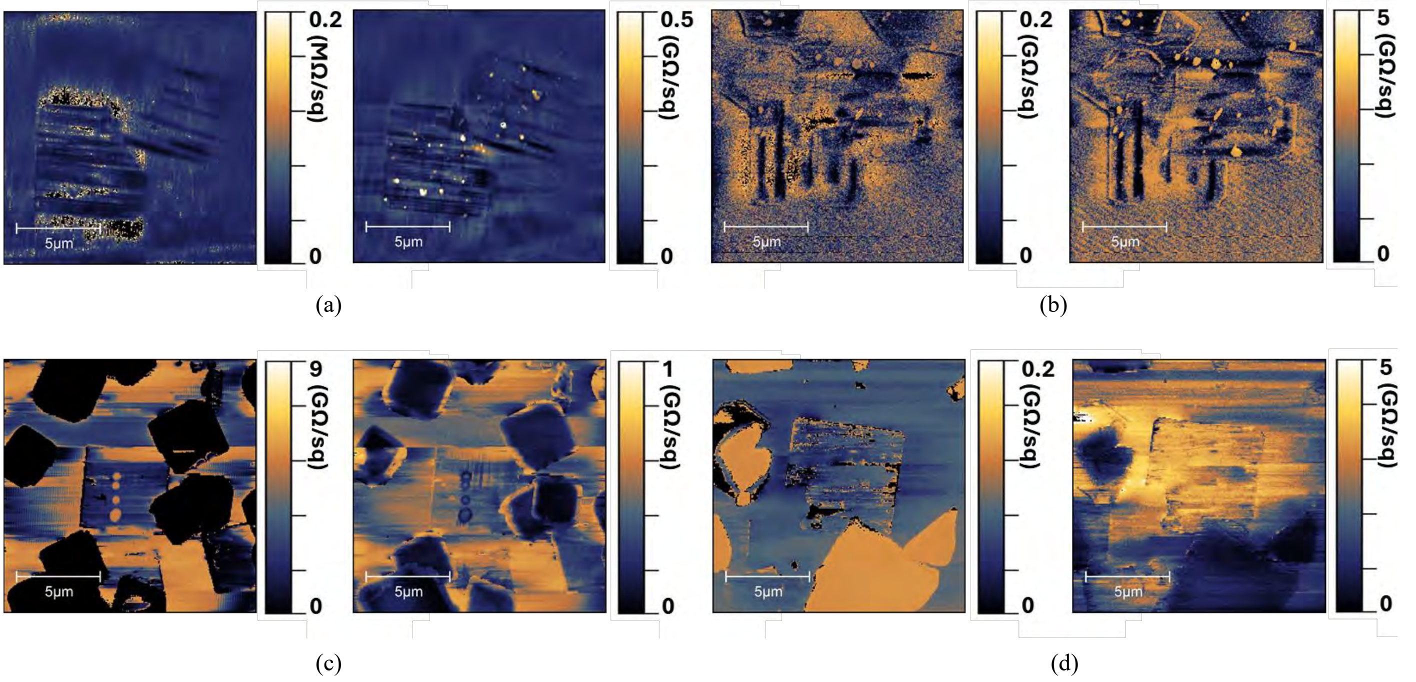

Fig. 3. (left) Manually vs. (right) automatically calibrated sheet-resistance images by SMM at 15.7 GHz of SnSe flakes of four different substrates on two different substrates: (a) 2.4 nm on SiO_2/Si, (b) 2.2 nm on SiO_2/Si, (c) 7.27nm on Si, and (d) 51nm on Si.

Therefore, (1) changes to:

$$S_{11,m} = (e_{00}^{base} \cdot G_{00}^{tip}) + (e_{01}^{base} \cdot G_{01}^{tip}) \frac{S_{11,a}}{1 - (e_{11}^{base} \cdot G_{11}^{tip}) S_{11,a}} \quad (5)$$

Thus, the machine model learns and predicts $[G_{00}^{tip} \quad G_{00}^{tip} \quad G_{11}^{tip}]$ to accelerate the calibration with prior confirmed static error coefficients, making real-time material property imaging possible.

E. Probe Geometry Prediction

SMM calibration requires precise prediction of error coefficients. After trials and errors, we found that the error coefficients in (5) must be accurate to at least the 4th decimal place. Otherwise, even minor deviations can propagate nonlinearly, leading to gross errors in admittance extraction. Traditional lightweight models such as Random Forest or Multi-Layer Perceptrons struggle to solve the complicated inverse problem.

Therefore, we use Tabular Prior-Data Fitted Network (TabPFN) pre-trained transformer-based model for tabular dataset prediction via in-context learning [13]. To handle the multi-output regression task, we implement a regressor chain architecture [14]. To emphasize the dependency among targets, we employ Gaussian Quantile Transformation [15], ensuring targets are predicted sequentially in a fixed chain order.

III. Results

To evaluate the proposed machine-learning automated calibration, we performed quantitative SMM imaging of R_{sh} on SnSe flakes of different thicknesses on both Si and SiO_2/Si substrates. Fig. 3 compares R_{sh} images obtained by manual calibration and by machine-learning automated calibration. The results demonstrate the latter's ability to consistently infer probe geometry on different substrates. Furthermore, automated calibration reveals more detailed features that are absent in manually calibrated images. This highlights the power of machine learning. While the extreme values and relative trends are consistent between the two calibration methods, there exists an order-of-magnitude systematic difference. This difference can be attributed to the limited size of the training datasets, which can be mitigated by expanding the training dataset with more diverse experimental ground-truth samples.

IV. Conclusion

This work introduces a TabPFN-based regressor-chain machine-learning automated calibration, which enables real-time material property imaging in SMM by decoupling static setup parasitic from dynamic probe geometry. This novel calibration approach can transform SMM from a niche research apparatus into a robust, high-throughput metrology tool. This approach can lower the entry barrier of SMM for users not experts in computational electromagnetics. Future development will focus on increasing precision by expanding the training dataset and by creating a comprehensive universal real-time imaging algorithm for the material characterization community in general.

Acknowledgment

This work was supported in part by in part by SUPREME, one of the seven centers sponsored by the Semiconductor Research Corporation and the U.S. Defense Advanced Projects

Agency through the Joint University Microelectronics Program 2.0 under Contract 2023-JU-3137 This work was performed in part at the Cornell NanoScale Facility, a member of NSF-sponsored NNCI under Grant NNCI-2025233.

REFERENCES

[1] G. Gramse, M. Kasper, L. Fumagalli, G. Gomila, P. Hinterdorfer, and F. Kienberger, "Calibrated complex impedance and permittivity measurements with scanning microwave microscopy," *Nanotechnol*., vol. 25, no. 14, p. 145703, Mar. 2014.

[2] M. Farina and J. C. M. Hwang, "Scanning microwave microscopy for biological applications: Introducing the state of the art and inverted SMM," *IEEE Microw. Mag.*, vol. 21, no. 10, pp. 52–59, Oct. 2020.

[3] L. Zheng, L. Shao, M. Loncar, and K. Lai, "Imaging acoustic waves by microwave microscopy: Microwave impedance microscopy for visualizing gigahertz acoustic waves," *IEEE Microw. Mag.*, vol. 21, no. 10, pp. 60–71, Oct. 2020.

[4] A. Morini, D. Mencarelli, A. Di Donato, G. Venanzoni, and M. Farina, "Calibration protocol for broadband near-field microwave microscopy," *IEEE Trans. Microw. Theory Techn.*, vol. 59, no. 10, pp. 2769–2776, Oct. 2011.

[5] M. Farina, X. Jin, G. Fabi, E. Pavoni, A. Di Donato, D. Mencarelli, A. Morini, F. Piacenza, R. Al Hadi, Y. Zhao, T. Pietrangelo, X. Cheng, and J. C. M. Hwang, "Inverted scanning microwave microscope for in vitro imaging and characterization of biological cells," *Appl. Phys. Lett.*, vol. 114, no. 9, p. 093703, Mar. 2019.

[6] R. C. Chintala, "Scanning microwave impedance microscopy: Room-temperature and low-temperature applications for device and material characterization," *IEEE Microw. Mag.*, vol. 21, no. 10, pp. 22–35, Oct. 2020.

[7] S. Berweger, T. M. Wallis, and P. Kabos, "Nanoelectronic characterization: Using near-field microwave microscopy for nanotechnological research," *IEEE Microw. Mag.*, vol. 21, no. 10, pp. 36–51, Oct. 2020.

[8] A. Tselev, "Near-field microwave microscopy: Subsurface imaging for in situ characterization," *IEEE Microw. Mag.*, vol. 21, no. 10, pp. 72–86, Oct. 2020.

[9] X. Wang, K. Nomoto, G. Fabi, M. Farina, D. Jena, H. G. Xing, and J. C. M. Hwang, "Quantitative scanning microwave microscopy for transfer characteristics of GaN high-electron-mobility transistors," *IEEE Trans. Microw. Theory Techn.*, vol. 73, no. 3, pp. 1573–1580, Mar. 2025.

[10] X. Wang, K. Nomoto, G. Fabi, R. Al Hadi, M. Farina, D. Jena, H. G. Xing, and J. C. M. Hwang, "Inverted scanning microwave microscopy of GaN/AlN high-electron mobility transistors," in *2024 103rd ARFTG Microwave Measurement Conference (ARFTG)*, 2024, pp. 1–4.

[11] Y. Zhang, X. Wang, J. C. M. Hwang, N. Mao, P. Wang, and J. Kong, "Characterization of in-plane polarization domains in 2D SnSe by scanning microwave microscopy," in *2025 104th ARFTG Microwave Measurement Symposium (ARFTG)*, 2025, pp. 1–4.

[12] X. Jin, J. C. M. Hwang, D. Mencarelli, L. Pierantoni, and M. Farina, "Nano probing for microwave engineers: Calculating probe-sample capacitance and charge distribution of a near-field scanning microwave microscope on a nanoscale," IEEE Microw. Mag., vol. 18, no. 1, pp. 71–75, Jan. 2017.

[13] M.-H. Chiu, X. Ji, T. Zhang, N. Mao, Y. Luo, C. Shi, X. Zheng, H. Liu, Y. Han, W. L. Wilson, Z. Luo, V. Tung, and J. Kong, "Growth of large-sized 2D ultrathin SnSe crystals with in-plane ferroelectricity," *Adv. Electron. Mater.*, vol. 9, no. 3, p. 2201031, Mar. 2023.

[14] P. García, J. de Curtò, I. de Zarzà, J. C. Cano, and C. T. Calafate, "Foundation models for cybersecurity: A comprehensive multi-modal evaluation of TabPFN and TabICL for tabular intrusion detection," Electronics, vol. 14, no. 19, p. 3792, Sep. 2025.

[15] E. Spyromitros-Xioufis, G. Tsoumakas, W. Groves, and I. Vlahavas, "Multi-target regression via input space expansion: Treating targets as inputs," *Mach. Learn.*, vol. 104, no. 1, pp. 55–98, Jul. 2016.

[16] F. Pedregosa *et al.*, "Scikit-learn: Machine learning in Python," *J. Mach. Learn. Res.*, vol. 12, pp. 2825–2830, Oct. 2011.